

# Towards Efficient Hyperdimensional Computing Using Photonics

Farbin Fayza\*, Cansu Demirkiran\*, Hanning Chen†, Che-Kai Liu‡, Avi Mohan\*  
Hamza Errahmouni†, Sangeon Yun†, Mohsen Imani†, David Zhang§, Darius Bunandar¶, Ajay Joshi\*¶

\*Boston University

†University of California, Irvine

‡Georgia Institute of Technology

§SRI International

¶Lightmatter

**Abstract**—Over the past few years, silicon photonics-based computing has emerged as a promising alternative to CMOS-based computing for artificial intelligence (AI)-based applications, in particular, Deep Neural Network (DNN)-based applications. Unfortunately, the non-linear operations and the high-precision requirements of DNNs make it extremely challenging to design efficient silicon photonics-based computing systems for DNN inference and training. Hyperdimensional Computing (HDC) is an emerging, brain-inspired machine learning (ML) technique that enjoys several advantages over existing DNN approaches, including (i) being lightweight, i.e., involving simple linear algebraic operations; (ii) requiring low-precision operands; and (iii) being robust to noise introduced by the nonidealities in the hardware. As the name suggests, HDC involves computation with vectors in very high-dimensional spaces. For HDC non-volatile memory (NVM)-based computing in-memory (CiM) approaches have been widely used, as CiM reduces the data transfer cost if the operand vectors can be fit into the memory. However, inefficient multi-bit operations, high write latency, and low endurance make CiM ill-suited for HDC. On the other hand, the existing electro-photonic DNN accelerators are inefficient for HDC because they are specifically optimized for matrix multiplication in DNN layers (e.g., convolutional or fully connected) and they consume a large amount of power because they need to use high-precision data converters.

In this paper, we argue that photonic computing and HDC complement each other better than photonic computing and DNNs, or CiM and HDC. We propose PhotoHDC, the first-ever electro-photonic accelerator for HDC training and inference, supporting the basic, record-based, and graph encoding schemes. Our novel accelerator microarchitecture leverages Mach-Zehnder Modulators and photodiodes to accelerate the encoding, bundling, and similarity measurement operations involved in HDC and use minimal electric circuitry for the rest of the system. Evaluating with popular datasets, we show that our accelerator can achieve two to five orders of magnitude lower EDP than the state-of-the-art electro-photonic DNN accelerators for implementing HDC training and inference. PhotoHDC also achieves four orders of magnitude lower energy-delay product than CiM-based accelerators for both HDC training and inference.

## I. INTRODUCTION

Silicon photonics-based computing is an emerging technology that is a promising alternative to CMOS-based computing for Artificial Intelligence (AI)-based applications [57]. A photonic chip can perform general matrix-matrix multiplication (GEMM) operations with significantly higher throughput and energy efficiency than an electronic chip [62]. Several recent

works have focused on accelerating Deep Neural Network (DNN) inference using silicon photonics and shown promising results [10], [38], [53], [54], [56], [62].

Though this photonics-based acceleration of DNNs is promising, there are a few limitations to this approach. First, DNNs contain a variety of non-linear operations (ReLU, GeLU, etc.). While linear operations can be efficiently performed in photonics, this is not the case for non-linear operations and they are typically performed using electronic circuits. Although the majority of DNN operations are linear, these nonlinear operations can easily become the bottleneck in the system as electronic circuits cannot easily match the high bandwidth of the photonic circuits. Second, the precision in photonic circuits is limited by the signal-to-noise ratio (SNR) we can achieve at the photonic circuit output and the precision of data converters that convert the signal between the digital (electronic) and analog (photonic) domains. Unfortunately, achieving high SNR in photonic circuits and high precision in data converters is expensive in terms of power consumption. While DNN inference is shown to be resilient to low precision, DNN training with backpropagation requires a much higher dynamic range in operations. This typically dictates that during training we need to use floating point operations—which cannot be efficiently performed using photonics. Essentially, to maximize the benefits of using silicon photonic technology for AI, we need to use a computing model that uses zero to a negligible number of non-linear operations and low-precision operands.

Hyperdimensional Computing (HDC) has recently emerged as a novel brain-inspired machine learning (ML) technique whose accuracy is close to DNNs in various applications, but it requires less computational resources than DNNs [14]. The HDC approach emulates neural processing in nature by mapping the sensory input data into a high-dimensional space as high-dimensional ( $\approx 10^4$ –*dimensions*) vectors called “hypervectors”. Both HDC training and inference mainly involve simple linear operations such as multiplication and addition on these hypervectors [58]. While the traditional DNNs rely on a deep and complex topology of networks and training via back-propagation, HDC focuses on significantly simpler architectures, which are computationally efficient and more interpretable [64]. Besides, HDC can successfully operate with

low precision (as low as a 1-bit precision) and still maintain good accuracy [48]. Previous works have shown that this HDC approach can be used in a variety of tasks including image classification, speech recognition, object tracking, face detection, and robotic tasks [14], [27], [41]. In addition, HDC is extremely robust to noise and can retain acceptable accuracy levels across a wide range of hardware failure rates in contrast to DNNs [31], [48].

Over the years, researchers have proposed a variety of CPU-based [24], GPU-based [28], ASIC-based [32], and FPGA-based [52] implementations for HDC [14]. However, with HDC being robust and operable with low bit-precision, Compute-in-Memory (CiM) has emerged as the most efficient approach for performing training and inference in HDC [29]. Lately, several Non-Volatile Memories (NVMs) fabrics have shown great potential for realizing efficient in-situ Matrix-Vector Multiplications (MVMs) in the form of content addressable memory (CAM) and crossbar [30], [36], [37], [42]. This creates an opportunity for accelerating HDC operations that can be rearranged as MVMs. CiM successfully eliminates the data movement cost [63] while efficiently performing computation and achieves a better performance in HDC compared to traditional Von Neumann architecture-based hardware accelerators, such as ASICs and FPGAs [8]. However, CiM is still not efficient for handling multi-bit operations, which is a hindrance to achieving satisfactory accuracy for complex classification tasks with HDC. Moreover, updating the values in an NVM array is costly and time-consuming ( $\approx$  hundreds of ns to  $\mu$ s) [59], [61]. While, for inference, this cost can be amortized by loading all the required values into the NVM array upfront and reusing them for multiple queries, these values need to be updated frequently for training, which causes a slowdown. One further problem is that for larger hypervector dimensions, it might not be possible to accommodate all the values on a single NVM-array chip, calling for external memory and thus incurring extra read/write operations for both training and inference.

Considering that HDC can tolerate low-precision operations and involves linear operations primarily, we argue that HDC and photonic computing complement each other perfectly. **In this paper, we propose—for the first time—using photonics for HDC inference and training.** The key contributions of our works are as follows:

- We, for the first time, propose using photonic computing for HDC applications. We argue that photonics and HDC make a good match as HDC mainly involves linear operations that can be performed efficiently in photonics and it is extremely resilient to low-precision operations.
- We propose PhotoHDC, a novel electro-photonic accelerator for HDC training and inference supporting three popular encoding schemes: traditional, record-based, and graph encoding. The accelerator microarchitecture utilizes Mach-Zehnder Modulators (MZMs) and PhotoDetector (PD) array to efficiently perform the encoding, bundling, and similarity measurement steps in HDC training and inference. The microarchitecture includes minimal electric circuitry, low-

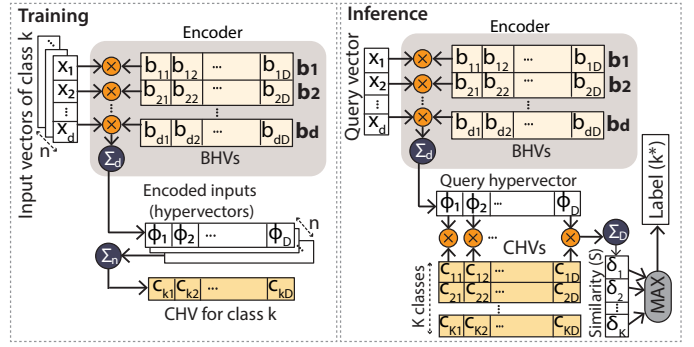


Fig. 1: An illustration of the HDC training and inference processes with the traditional encoding scheme.

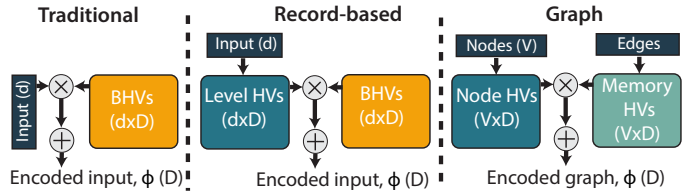


Fig. 2: An overview of three HDC encoding schemes: traditional, record-based, and graph encoding.

precision data converters, and memory units.

- We introduce novel dataflows, designed to work with each encoding scheme, for both HDC training and inference on PhotoHDC.

We evaluate the performance of PhotoHDC on a variety of datasets that are frequently employed in HDC research. We map HDC to three popular State-Of-The-Art (SOTA) electro-photonic accelerators for DNNs, ADEPT [10], AL-BIREO [53], and DEAP-CNN [7], and provide a comprehensive comparison highlighting the limitations of these accelerators. For both HDC training and inference, our proposed accelerator achieves two to five orders of magnitude lower Energy-Delay Product (EDP) than SOTA electro-photonic DNN accelerators. We also compare PhotoHDC with CiM-based accelerators. PhotoHDC achieves four orders of magnitude lower EDP than CiM-based accelerators for both HDC training and inference.

## II. BACKGROUND

### A. HDC Overview

As described earlier, HDC emulates neural processing in nature by mapping data into hypervectors. Like DNNs, HDC consists of training and inference. Below we describe the training and inference processes in HDC.

1) *Training*: The training process in HDC involves mapping training data to a high-dimensional space, and combining the resulting *hypervectors* class-wise to generate a prototypical representative class hypervector (CHV) for each class. In this paper, we will investigate three major encoding schemes: “traditional” encoding [19], [33], [34], “record-based” encod-

ing [23], [24], [31] and “graph” encoding [43], [46]<sup>1</sup>. The rest of this subsection is organized as follows. We first describe the training and inference processes in detail using traditional encoding, and later explain record-based encoding and graph encoding while highlighting how they differ from traditional encoding.

In Figure 1 on the left side, we show an overview of the training process with traditional encoding. Throughout this subsection, we will assume that the classification problem at hand comprises  $K$  classes and we want to generate the CHV of class  $k$ , where  $k \in [K]$ . We can generate the CHV of class  $k$  with the following two steps.

**Traditional Encoding:** In this step, we map all the input vectors in the training dataset that belong to class  $k$  from a low-dimensional space  $\mathcal{X} \subset \mathbb{R}^d$  to a high-dimensional space  $\mathcal{H} \subset \mathbb{R}^D$ , using a (typically *randomized*) function  $\phi: \mathcal{X} \rightarrow \mathcal{H}$ . The top half of Figure 1 (left side) illustrates this process. For example, given an input vector  $\mathbf{x} \in \mathcal{X}$ , and IID (Independent and Identically Distributed) sampled vectors  $\{\mathbf{b}_1, \dots, \mathbf{b}_d\}$  from  $\mathcal{H} = \{\pm 1\}^D$ , the encoder  $\phi$  is defined as

$$\phi_j(\mathbf{x}) = \sum_{i=1}^d b_{ij}x_i, \quad 1 \leq j \leq D \quad (1)$$

$$\Rightarrow \phi(\mathbf{x}) = B^T \mathbf{x}, \quad (2)$$

where,  $B_{(d \times D)} = [\mathbf{b}_1, \dots, \mathbf{b}_d]^T$  is the encoding matrix, the vectors  $\{\mathbf{b}_1, \dots, \mathbf{b}_d\}$  are the base hypervectors (BHVs),  $\mathbf{x} = [x_1, \dots, x_d]^T$  and  $b_{ij}$  is the  $j^{\text{th}}$  coordinate of the  $i^{\text{th}}$  BHV. In other words, we multiply each feature of the input vector  $\mathbf{x}$  with a corresponding hypervector, and add the results element-wise to generate the input hypervector. Equation (2) shows that the encoding operation can be represented as a matrix-vector multiplication between the encoding matrix  $B_{(d \times D)}$  and the input vector  $\mathbf{x}_{(d \times 1)}$ . Let us assume that we have  $n$  such input vectors for class  $k$ , encoded to  $n$  input hypervectors using Equation (2).

**Bundling:** After the encoding step is completed, we add the  $n$  input hypervectors element-wise to generate the CHV of class  $k$ . In HDC parlance, such element-wise addition operations are called “Bundling” [58]. After bundling, we normalize the result to fit the CHV elements within the desired bit size.

We follow this two-step process for each class in  $K$  to generate all the CHVs. This training scheme is called “single-pass” training. Formally, if the training dataset  $\mathcal{D}_{tr}$  is partitioned class-wise as  $\mathcal{D}_{tr} = \bigcup_{k=1}^K \mathcal{D}_k$ , then in single-pass training, the CHVs  $\{\mathbf{c}_1, \dots, \mathbf{c}_K\} \in \mathbb{R}^D$  are generated using

$$\mathbf{c}_k := \sum_{\mathbf{x} \in \mathcal{D}_k} \phi(\mathbf{x}), \quad k \in [K]. \quad (3)$$

Single-pass training is the basic and most commonly used training method. Other specialized methods, such as online training, update the CHVs as and when more training data becomes available i.e., in an “online” fashion [19]. However,

<sup>1</sup>The literature contains a fourth scheme called “N-gram-based” encoding which our current architecture doesn’t support. Providing support for this fourth scheme will form part of our future work.

these specializations are outside the scope of the current article and will be the focus of future work.

2) *Inference:* Once training is complete, we can classify a query input by first encoding it to  $D$ -dimensional space using the same BHVs used in training, then calculating similarity with each CHVs generated by the training step (shown in Figure 1 on the right side). There can be different types of similarity metrics such as the inner product, cosine similarity, and Hamming distance. We use the cosine similarity metric in this work. The class with the highest similarity score indicates the label for the query input. Specifically, inference is performed through the following two steps.

- 1) The query input vector  $\mathbf{x} \in \mathcal{X}$  (whose class we do not know) is encoded to its corresponding query hypervector  $\phi(\mathbf{x}) \in \mathcal{H}$ . This encoding step is the same as the encoding step done during training (see Figure 2).
- 2) Using a *similarity metric*  $\delta: \mathcal{H} \times \mathcal{H} \rightarrow \mathbb{R}$ , we determine  $k^*$ , the class with the most similar CHV. This  $k^*$  class is determined as follows:

$$k^* := \operatorname{argmax}_{k \in [K]} \delta(\phi(\mathbf{x}), \mathbf{c}_k) \quad (4)$$

The inference step can be further simplified as follows. Let  $C := [\mathbf{c}_1, \dots, \mathbf{c}_K]_{(K \times D)}^T$  and  $\mathbf{s} = [\delta_1, \delta_2, \dots, \delta_K]_{K \times 1}^T$ . Then, all  $K$  similarities can be simultaneously generated as

$$\mathbf{s} = C\phi(\mathbf{x}) \quad (5)$$

Equations (2) and (5) show that encoding and similarity checking, the two primary operations in HDC, can both be represented as MVMs. Note that this simplification is possible only due to our choice of the encoder ( $\phi(\cdot)$ ) and similarity metric ( $\delta(\cdot)$ ).

3) *Other Encoding Schemes:* As stated earlier, our accelerator can support two other schemes— record-based and graph encoding. Note here, that the basic flow of the procedure still remains the same. For training, we encode an input feature to produce the associated hypervector, follow it up with a bundling operation that generates class hypervectors, and during inference, we follow the max of inner products over all the class hypervectors. The only change is the method of encoding the given feature vector. Figure 2 succinctly illustrates the differences in the three encoding procedures.

**Record-based Encoding:** This employs two types of hypervectors, representing the feature position (*position* hypervectors) and value of said feature (*value* hypervector) [14]. The  $d$  position hypervectors  $\mathbf{b}_1, \dots, \mathbf{b}_d$  are generated IID to encode the feature position information in a feature vector. The feature value information is quantized to  $m$  level hypervectors  $\{\mathbf{L}_1, \dots, \mathbf{L}_m\}$ . Suppose the level hypervectors associated with a given input  $\mathbf{x}$  are  $\mathbf{L}_{1,x}, \dots, \mathbf{L}_{d,x}$  (where  $\mathbf{L}_{i,x} \in \{\mathbf{L}_1, \dots, \mathbf{L}_m\}, 1 \leq i \leq d$ ), then the final encoding hypervector for input  $\mathbf{x}$  is given by

$$\mathcal{H}(\mathbf{x}) = \sum_{i=1}^d \mathbf{L}_{i,x} \oplus \mathbf{b}_i, \quad (6)$$

where  $\oplus$  represents element-wise XOR, which is replaced with multiplication in case of multi-bits.

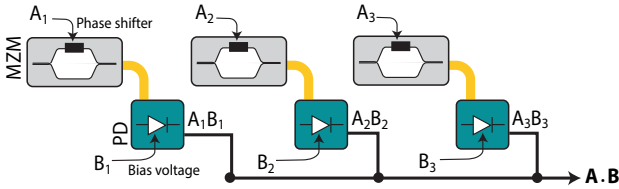


Fig. 3: Dot product of vectors  $\mathbf{A}$  and  $\mathbf{B}$  using MZMs and PDs.

**Graph Encoding:** This encoding technique is specific to problems such as social network analysis, genomics, and knowledge graph representations, where the input data structure is a graph [46]. The challenge here is to associate with an input graph  $G = (\mathcal{V}, \mathcal{E})$  a hypervector that encodes the structure of the graph, i.e., the information within  $\mathcal{E}$ . Towards this end, a set of hypervectors  $\mathbf{b}_1, \dots, \mathbf{b}_V$ , called node hypervectors, are generated IID, where  $V = |\mathcal{V}|$ . Next, with every node  $i \in \mathcal{V}$ , another hypervector  $\mathbf{m}_i$ , called memory hypervector, is associated that encodes the neighborhood of node  $i$ . So, for every  $i \in \mathcal{V}$ ,  $\mathbf{m}_i = \sum_{j:(i,j) \in \mathcal{E}} \mathbf{b}_j$ . A bundling operation then generates the encoding hypervector for this graph as follows

$$\mathcal{H}(G) = \frac{1}{2} \sum_{i \in \mathcal{V}} \mathbf{b}_i \oplus \mathbf{m}_i, \quad (7)$$

The  $1/2$  accounts for the fact that every edge in  $\mathcal{E}$  is counted twice in the above calculation. This basic technique can be extended in a fairly straightforward manner to incorporate edge weights and directed graphs. For details, we refer the reader to [46]. Note that the graph encoding scheme follows the same process as record-based encoding once we have generated the node hypervectors and the memory hypervectors.

### B. Photonic Computing Overview

In our work, we utilize Mach-Zehnder Modulators (MZMs) and PhotoDetectors (PDs) to perform vector dot products. An MZM can attenuate the amplitude of an optical signal. Inside an MZM, a silicon waveguide carrying an input signal is split into two arms. By changing the phase of the optical signal in one arm, and then recombining optical signals in the two arms, we can achieve interference, leading to amplitude modulation of the input signal. The desired phase difference in an arm can be obtained by delaying the light in that arm, which can be achieved via a variety of techniques, such as thermo-optic effect [18], mechanical effect [13], or electric-field induced electro-optic effect [47]. The MZM we use in our work operates on the principle of the electro-optic effect.

PD is a commonly used component of electro-photonic chips that can convert an optical signal to an electrical signal. A PD is a light-sensitive diode that generates current (called photocurrent) when exposed to optical signals of sufficient power. The photocurrent is proportional to the power of the incident optical signal. By applying a bias voltage across a PD, one can control the maximum photocurrent that gets generated.

Figure 3 shows how we can perform dot product of two vectors  $\mathbf{A} = [A_1, A_2, A_3]$  and  $\mathbf{B} = [B_1, B_2, B_3]$  with MZMs and PDs. First, we modulate the light waves through three MZMs by controlling the phase shifters using  $A_1, A_2$ , and  $A_3$ .

We direct the modulated light waves towards the PDs, which we control with the bias voltages to generate photocurrent proportional to  $B_1, B_2$ , and  $B_3$ . Therefore, we obtain currents representing  $A_1 \cdot B_1, A_2 \cdot B_2$ , and  $A_3 \cdot B_3$  at the output of the PDs. We accumulate the currents in a single wire to perform a summation operation of the multiplication results, and thus, complete the dot product of  $\mathbf{A}$  and  $\mathbf{B}$ . This basic device-level idea of utilizing MZMs and PDs for performing MAC operations was first proposed by Harris [17]. In our work, we leverage this idea to architect a novel vector dot product unit which is a key building block of PhotoHDC.

## III. ELECTRO-PHOTONIC ACCELERATOR FOR HDC

This section delves into the microarchitectural details of our proposed accelerator, PhotoHDC. We first introduce the high-level design of the PhotoHDC microarchitecture and discuss the individual components in detail. Then we explain the dataflow to perform training and inference with traditional and record-based encoding using PhotoHDC. We do not describe the dataflow for graph encoding; as mentioned earlier, the training and inference with graph encoding are the same as record-based encoding, assuming that we have the node and memory hypervectors ready.

### A. PhotoHDC Microarchitecture

Figure 4 presents an overview of the PhotoHDC accelerator, which primarily comprises an  $R \times C$  photonic unit, data converters, switches, and adders. The photonic unit contains PDs and MZMs to perform MAC operations. It is also connected to memory units for storing the BHVs, CHVs, inputs, intermediate results, and final results. We provide a detailed description of each component below.

1) *Lasers:* The optical signals required for the accelerator are generated using off-chip lasers and guided by a single-mode fiber. There are  $C$  lasers in an  $R \times C$  photonic unit. The light from each laser is coupled to a waveguide via couplers and fed to an MZM.

2) *MZMs:* An  $R \times C$  unit contains  $C$  MZMs, one for each column. These MZMs are responsible for modulating the optical signals to represent the values in BHVs or CHVs, depending on the ongoing operation (training or inference with traditional or record-based encoding) in the accelerator. The modulated optical signal from each MZM is propagated to all rows in the corresponding column with the waveguides split in a binary tree manner. The columns are optically isolated from each other.

3) *PD Array:* The core component of the accelerator is a 2D array of PDs. The  $R \times C$  photonic unit in Figure 4 contains an array of  $R$  rows and  $C$  columns of PDs. The bias voltages of the PDs are adjusted based on the operands that are required for the MAC operation with the BHVs or CHVs. These operands can be input feature values, level hypervectors, or encoded data depending on the accelerator operation, and cannot fit within a single  $R \times C$  unit. So we partition the operand values into multiple  $R \times C$  tiles, and program them to the PD array one tile at a time. After

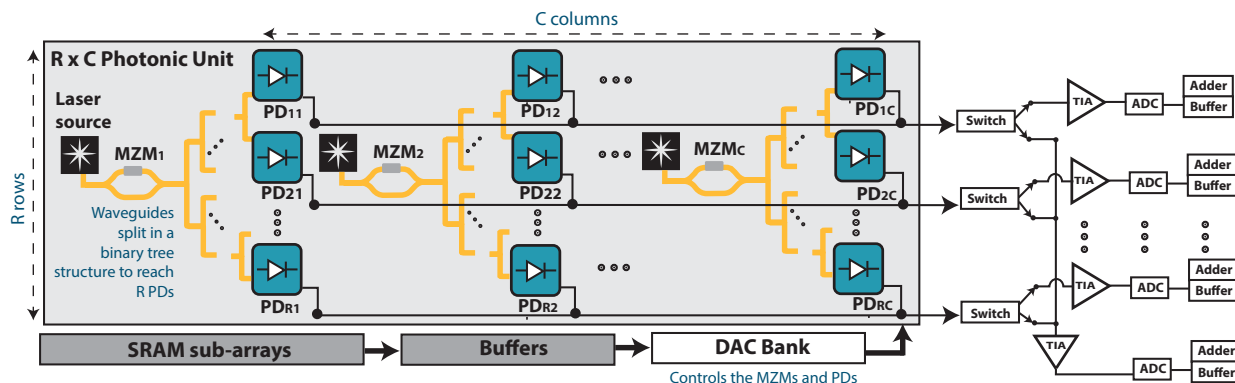


Fig. 4: Overview of the PhotoHDC accelerator microarchitecture consisting of an  $R \times C$  photonic unit, data converters, memory units, and other circuits. The photonic unit uses one MZM per column to modulate the BHVs or CHVs and a PD array of  $R$  rows and  $C$  columns to perform multiplication with corresponding input values.

the PDs are programmed, each PD receives the modulated optical signal from the MZM of the corresponding column and generates photocurrent according to the optical power and the bias voltage, effectively performing a multiplication operation between the values represented with the MZM and the PD. The output currents (multiplication results) of the PDs in a row are accumulated by a wire, which is connected to a switch that routes the current to the appropriate destination, based on the accelerator operation.

4) *Switches*: We have one switch per row in our accelerator. The role of a switch is to either forward the current to the associated Trans-Impedance Amplifier (TIA) or to a wire that accumulates the currents coming from all the rows. This accumulation helps us efficiently perform the bundling operation in training, which we describe in the next subsection.

5) *Data Converters*: As described in Section II-B, the MZMs and the PDs are programmed or controlled by analog voltages. Therefore, the operands, which are stored in the SRAM arrays as digital values, need to be converted into the analog domain using Digital-to-Analog Converters (DACs). An  $R \times C$  unit requires  $C$  DACs for the MZMs and  $R \times C$  DACs for the PD array.

At the end of each row, we receive the output current representing the result of the MAC operation and convert the output into digital values. For this conversion, we first use TIAs to convert the currents into voltages and then ADCs to generate the digital value. We have one TIA and one ADC in every row, and one additional TIA and ADC dedicated for converting the summed current of all the rows into a digital value.

6) *Adder-Buffer Units*: After each ADC, we include CMOS-based digital adders and buffers to accumulate the partial results when necessary. Specifically, if the operating frequency of the photonic unit is  $f$  GHz, we have  $f$  adders in each adder-buffer unit assuming that an adder can perform addition in 1 ns. The buffers included with the adders hold the operands and the adders' outputs.

7) *Memory Units*: We use SRAM arrays to store the BHVs, CHVs, and two batches of input vectors. We need space to

store two batches of input vectors because we use the double-buffering approach where while processing a batch, we load the next batch of inputs from an external DRAM to ensure smooth data processing with no data movement delays. In the case of record-based or graph encoding, we store the level hypervectors in a look-up table SRAM.

We include a buffer to store the elements of the upcoming tile to be programmed into the PD array. This buffer enables us to load the data from the SRAM array while the operations in the MZI array continue and minimize the data transfer latency between consecutive tiles. We also use buffers to store the partial outputs.

## B. PhotoHDC Functionality and Dataflow

1) *Training with Traditional Encoding*: We employ an input-stationary approach for performing HDC training with traditional encoding. The key idea is to load the inputs tile by tile into the PD array and complete all computations (both encoding and bundling) required for each tile before proceeding to the next. Figure 5a provides a detailed illustration of this dataflow. We program the  $R \times C$  PD array with  $C$  feature values of  $R$  samples ( $x^1 \dots x^R$ ) at a time. Subsequently, we employ the MZMs to modulate the corresponding  $C$  elements of each hyperdimension of the BHVs in every cycle. Therefore, each row's output is the partially encoded data pertaining to the  $C$  feature values of each sample. For example, in the figure, we load the first  $R \times C$  input tile into the PD array, and modulate corresponding  $C$  rows of the BHV matrix,  $b_{11}$  to  $b_{c1}$ , through the MZMs in the first cycle. This generates the partial encoding of the first hyperdimension,  $\phi_1$ , involving the first  $C$  feature values for the  $R$  samples. In the next cycle, we modulate the second column of the BHV matrix,  $b_{12}$  to  $b_{c2}$ , with the same input tile existing in the PD array, and so on.

To bundle the partial encoding results, we control the switches to direct the row currents to a wire for accumulation. Assuming that the  $R$  samples belong to class  $k$ , the summed current represents partial CHV of class  $k$ . This current is converted to digital value with an ADC and stored in a buffer.



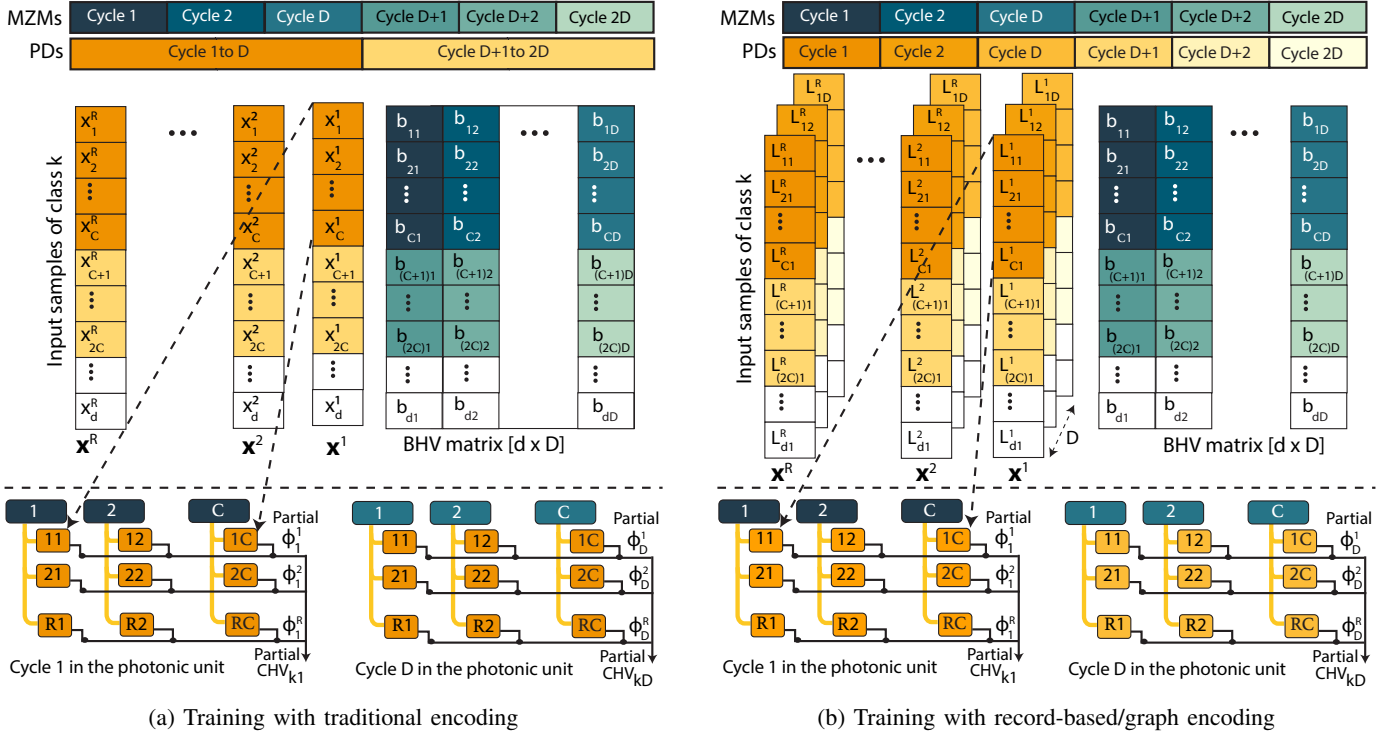
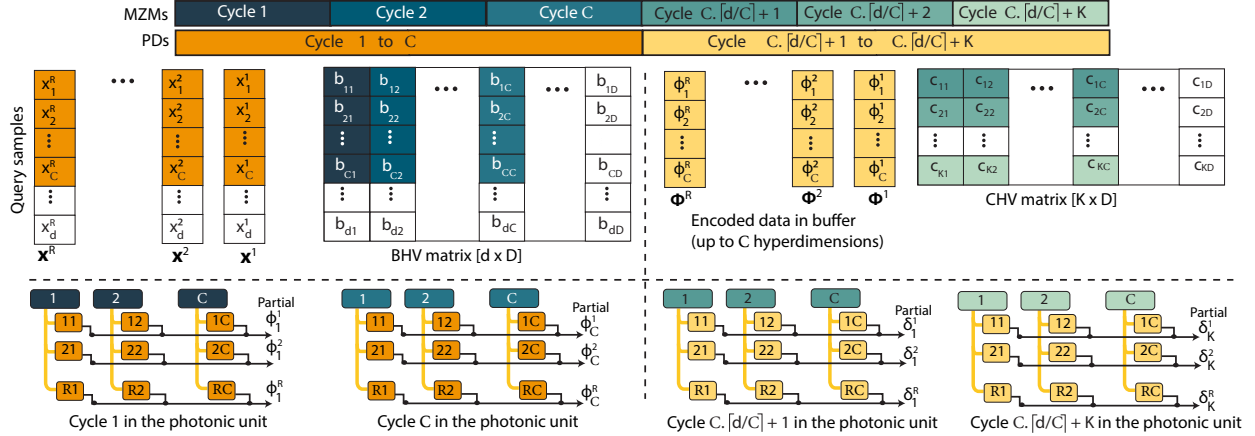


Fig. 5: Dataflow of HDC training with PhotoHDC for traditional and record-based/graph encoding methods. The PD array processes the input values tile by tile, and for each tile, the MZMs modulate the corresponding BHV portions. Partial encoding results are generated in every row and bundling is performed by summing the row currents.



Thus, in every cycle, we compute both encoding and bundling of  $R$  samples involving  $C$  features in a single hyperdimension. We spend  $D$  cycles to finish working with all  $D$  dimensions for the loaded input tile.

We repeat the same procedure for the next  $C$  feature values of the  $R$  input samples and the results are added to the partial CHV results generated for the previous tile. As there are  $d$  feature values in the input samples, it would take  $\lceil d/C \rceil \times D$  cycles to complete the encoding and bundling of  $R$  samples. If we have multiple photonic units, we can distribute the input tiles among the units and process them in parallel. Once we are done processing all the training samples, we write the final CHVs in the SRAM.

2) *Training with Record-based Encoding*: We follow a similar procedure as traditional encoding for record-based encoding. However, in record-based encoding, for each  $d$  feature of an input vector, we have a  $D$ -dimensional level hypervector. Therefore, one input feature value is not shared with all the hyperdimensions of the BHVs like the traditional encoding. Each time we load a different column of the BHV matrix to the MZMs, we must switch the input tile in the PDs accordingly. We demonstrate this process in Figure 5b. In the figure, we load the first  $C$  elements of the first column of the BHVs into the MZM, and the corresponding  $C$  elements from the level hypervectors of the  $R$  samples into the PDs. Unlike traditional encoding, we cannot keep this input tile in the PDs

for the next  $D - 1$  columns because for each hyperdimension we need to load the corresponding level hypervector tile. So we switch the tile accordingly every cycle and the rest of the procedure is similar to the traditional encoding during training. The amount of computation is the same as the traditional encoding and it takes the same  $\lceil d/C \rceil \times D$  cycles to complete the encoding and bundling of  $R$  samples.

3) *Inference with Traditional Encoding*: Figure 6 shows the inference dataflow with PhotoHDC for traditional encoding. As described in Section II-A, for inference, we need to first encode the input sample, then calculate the similarity scores between the encoded sample and all the CHVs to get the class label. The mapping strategy of encoding during inference involves loading the inputs in the PD array and the BHVs in the MZMs similar to the encoding method during training. We process  $R$  samples at a time. Similar to training, in  $R$  rows of the PD array, we map  $C$  feature values of  $R$  samples and modulate the corresponding BHV portions. However, as we do not need to bundle the encoded samples during inference, we need to handle each row with separate ADCs. In the photonic unit shown in Figure 6, we can see that the rows are not merged in a wire. We control the switch to direct the output of each row to the ADC corresponding to that row, therefore, keeping the results of each row separate. We keep the input tile in the PD array for  $C$  cycles and process  $C$  columns of the BHVs for the corresponding tile. Repeating this for all  $d$  rows of the  $R$  samples takes  $\lceil d/C \rceil \times C$  cycles. We store the results in an  $R \times C$  buffer and add the partial results whenever ready. When we are done handling  $C$  hyperdimensions for the  $R$  samples, we have the  $R$  encoded samples up to the  $C$  hyperdimensions in the buffer (shown in the right side of Figure 6).

We use the next  $K$  cycles to perform similarity measurements with the  $K$  CHVs for the corresponding  $C$  hyperdimensions we encoded. We load the encoded  $R \times C$  tile from the buffer to the PD array and modulate the CHVs for each class one at a time with the MZMs. Thus, we generate an output of shape  $R \times K$ , containing the partial similarity scores for all classes for the  $R$  samples. We store this result in another buffer and repeat this process for all  $D$  hyperdimensions ( $C$  hyperdimensions at a time). After a total of  $\lceil D/C \rceil \times ((\lceil d/C \rceil \times C) + K)$  cycles, we get the final similarity scores for the  $R$  samples. By calculating the maximum class scores for the  $R$  samples, we get  $R$  labels and complete a batch inference.

4) *Inference with Record-based Encoding*: The only difference between doing inference with record-based encoding and traditional encoding is the encoding part. We follow the same record-based encoding procedure mentioned in the training section without bundling the encoded samples for inference. The rest of the procedure is the same as the inference procedure described for traditional encoding. The number of cycles is again,  $\lceil D/C \rceil \times ((\lceil d/C \rceil \times C) + K)$ , for a batch inference of  $R$  samples.

### C. Performance vs. DAC area tradeoff

As mentioned in Section III-A, an  $R \times C$  photonic unit requires  $R \times C$  DACs for the PD array and  $C$  DACs for the MZMs. This large DAC count significantly increases the area of the chip. To reduce the number of DACs, we introduce an extra delay of  $t_{DAC}$  cycles, before switching a tile in the PD array. During this extra period, each DAC can program multiple PDs. As a result, we can reduce the number of DACs that we need, in turn reducing the PhotoHDC area. This extra delay has minimal impact on performance for training and inference with traditional encoding, where we do not switch the tiles frequently. However, in record-based encoding, we have to switch the tile every cycle, therefore, adding a delay before switching is equivalent to operating at a lower frequency. So we do not add any  $t_{DAC}$  delay for record-based encoding. We show the trade-off between area improvement and performance loss for this delay in detail in Section V for traditional encoding.

## IV. EVALUATION METHODOLOGY

In this section, we provide a detailed description of the methodology that we used for calculating the Power/energy, Performance, and Area (PPA) of PhotoHDC. We also describe how we mapped HDC training and inference in three SOTA electro-photonic accelerators for DNN, and CiM-based designs of HDC accelerators.

### A. PPA Estimation of PhotoHDC

1) *Power/Energy Estimation*: In PhotoHDC, power is consumed by SRAM read-writes, adders, data conversions, E-O and O-E conversions, and the laser. We generate the SRAM arrays with an SRAM compiler for the GF22FDX technology node [2] to estimate the energy consumption per read and write operation. We count the total number of SRAM reads and writes during operations and calculate the SRAM energy. For addition operation in PhotoHDC, we design a 32-bit adder using RTL and synthesize it using Genus [1] with the GF22FDX technology node.

To guarantee  $b$ -bit precision at the PD output, a signal-to-noise ratio (SNR) of at least  $2^b$  should be preserved within the optical path. The optical signal power at a PD needs to be  $(\kappa \text{SNR}_{\text{shot}})^2 \cdot (q \Delta f/4)$ , where  $\text{SNR}_{\text{shot}}$  is the SNR with respect to the shot noise,  $\kappa$  accounts for all other noise contributions such as thermal noise,  $q$  is the elementary charge, and  $\Delta f$  is the bandwidth of the detector [10]. We consider noise factor of 3, a fiber-to-chip coupling loss of 2 dB [10], a loss at the MZMs of 1.2 dB [4], PD responsivity 1.05 A/W [21], and a laser efficiency of 20% [40]. Accounting for all the losses and inefficiencies, we calculate the total laser power required for an  $R \times C$  photonic unit. The modulation with the MZMs consumes  $\sim 20$  fJ/bit [55], and the tuning circuits of the MZMs consumes 11.3mW [4]. TIAs consume 75 fJ/bit [49].

Using the energy numbers of a 14-bit DAC [20] and a 10-bit ADC [15] of 28 nm technology node, we apply technology scaling to estimate the energy consumption of the lower

precision output ADCs, input DACs, and weight DACs. Both DAC and ADC energy consumption scales roughly with  $2^{\text{ENOB}}$  where ENOB is the effective number of bits of the converter. We use this approach as there are no publicly available DAC and ADC implementations or prototypes in GF22FDX with our desired bit precision and throughput.

2) *Latency Estimation*: In Section III-B, we describe each dataflow in detail and the corresponding cycle counts for R number of samples. Using those cycle counts, according to the accelerator frequency, we calculate the total training latency considering all training samples and the inference latency for the total number of inferences.

3) *Area Estimation*: For SRAM and the adders, we estimate the area with the GF22FDX technology node [2]. The area of the abovementioned ADCs and DACs are scaled down to 22 nm technology node assuming a fixed voltage scaling. Each MZM is  $300 \times 50 \mu\text{m}^2$  [4] and the area of a PD is  $4 \times 50 \mu\text{m}^2$  [21].

### B. HDC with SOTA Electro-Photonic Accelerators

We map HDC training and inference in SOTA electro-photonic accelerators for DNNs. Below we describe how we mapped the dataflow to these accelerators.

1) *ADEPT*: ADEPT [10] performs DNN inferences by expressing linear layers (convolution or Fully-Connected (FC) layer) as MVMs and utilizing MZI arrays for efficient computation. Weight tiles are programmed into the MZI arrays using SVD decomposition and phase shifter control. Inputs are then modulated with MZMs and passed through the MZI arrays to perform MVM. CMOS-based vector processing units handle partial outputs and non-linear operations.

For training with traditional encoding on ADEPT, we perform encoding and bundling in a two-stage pipelined manner. We utilize the MZI arrays to encode the inputs with an MVM of the BHVs (as weights in the MZI array) and the input vector. Then, we bundle the encoded inputs using the adders of the vector processing units. Likewise, for inference, we first encode the input samples in a similar manner as training, then perform MVM of the CHVs (weights) and the encoded input to calculate similarity scores. We use a  $128 \times 128$  MZI array as suggested in the ADEPT paper for both encoding and similarity measurement.

Performing record-based encoding is inefficient in an MZI array, because it cannot be represented as an MVM operation. We can at most use one row of the MZI array if we want to handle the BHV matrix column by column instead of tile by tile.

2) *ALBIREO*: ALBIREO [53] accelerates the convolution operations of DNNs by utilizing MZMs to multiply one weight vector with multiple input vectors represented with light waves of different wavelengths simultaneously. To handle the multiplication results of different input vectors separately, there is a 2D array of MRRs, where each MRR in a row couples with light waves of unique wavelengths, thus, enabling parallel dot product of multiple input vectors. For an FC layer,

ALBIREO uses only one column of the MRR array as there is no parameter sharing in FC layers like convolution.

With traditional encoding, HDC encoding and similarity measurement are equivalent to the operation of an FC layer. Therefore we follow the dataflow of FC layers described in the Albireo paper for HDC operations. We use the configuration for the 60 W version of Albireo. Here too, similar to ADPET, we assume that there are two similar cores, and the encoding and similarity measurement steps are pipelined for inference. Record-based encoding can be mapped in a similar manner by performing one dot product at a time. For both encoding schemes, ALBIREO suffers from low utilization due to the limitation of using only one column in the MRR array.

3) *DEAP-CNN*: DEAP-CNN [7] employs an MRR weight bank approach to perform efficient convolution operations. The authors use two MRR banks: one to modulate the weights (kernels), and another to modulate the corresponding input pixels. Through wavelength division multiplexing (WDM), each input in a row gets paired with the corresponding kernel value in the kernel bank, and thus a dot product is performed.

We can perform traditional encoding by modulating the BHVs in the kernel bank and the inputs in the input bank to perform dot product between them. During inference, we can first encode a batch of samples and then calculate the similarity scores by loading the CHVs in the kernel bank and the encoded data in the input bank in a similar manner. We follow the same pipelining assumption as the previous two accelerators. We use the 1024 MRR design with two units that consume 100 W power as mentioned in the paper.

If we want to perform record-based encoding with DEAP-CNN, the procedure would be similar, but we would need to change the kernel weight bank values that hold the BHVs every cycle. As a result, the tuning power would rise, making the system inefficient.

### C. HDC with CiM-based Accelerator

We compare the performance of PhotoHDC with CiM-based accelerators. We modify DNN-NeuroSim [39], [44], [45] for estimating NVM-based HDC training and inference acceleration performance [37] with ReRAM crossbar array. We regard the HDC encoding and similarity measurement as one fully connected DNN layer and modify the network configuration file in the simulator accordingly. Specifically, we use DNN-NeuroSIM v1.3 to simulate encoding and cosine similarity measurement, and DNN-NeuroSIM v2.1 to simulate the CHV update on the CiM platform. Note that DNN-NeuroSIM v2.1 generates the results for the complete training of a DNN layer including the forward pass, error calculation, gradient calculation, and weight update. We only use the weight update latency and energy to get the cost of the CHV update.

We adopt a 22nm technology node similar to PhotoHDC for a fair comparison. For the ReRAM crossbar array, we use  $128 \times 128$  subarray size and SAR-ADCs. We choose  $128 \times 128$  because this size has been shown to achieve relatively balanced trade-offs among accuracy, energy efficiency, throughput, area,



TABLE I: Datasets used for evaluation.

Dataset	$d$	$K$	Train size	Description
ISOLET [12]	617	26	6238	Alphabet recognition from voice
UCIHAR [6]	561	12	6231	Human activity recognition
FACE [5]	608	2	522441	Gender detection from images
PAMAP [50]	75	5	611142	Activity Recognition (IMU)
PECAN [3]	312	3	22290	Urban Electricity Prediction
Avg. # vertices	$K$	Train size	Description	
DD [11]	285	2	1178	Classify proteins
ENZYMES [9]	33	6	600	Classify enzymes
PROTEINS [11]	40	2	1113	Classify proteins

TABLE II: Impact of  $R$  and  $C$  on the power consumption.

Component	$2\times$ Increase in $R$	$2\times$ Increase in $C$
MZMs	$1\times$	$2\times$
Lasers	$2\times$	$2\times$
SRAM arrays	$2\times$	$2\times$
DACs for MZMs	$1\times$	$2\times$
DACs for PDs	$2\times$	$2\times$
ADCs (training)	$1\times$	$1\times$
ADCs (inference)	$2\times$	$1\times$

and memory utilization [45]. For CiM too, we follow the same pipelining strategy as the SOTA electro-photonic accelerators in training and inference.

#### D. Datasets, Hyperdimension, and Bit-Precision

We list the datasets used for evaluation in Table I. The columns  $d$  and  $K$  show the number of input features and the number of classes, respectively. The train size column shows the number of samples used for training, which is chosen to be 70% of the original dataset size. For traditional and record-based encoding, we use the first five datasets. The bottom three are graph datasets and we use them for graph encoding. We choose these datasets due to their popularity in HDC research [19] [31] [43] [34] [64], and their diversity. We use 4-bit precision with  $D = 4096$  in all our experiments. Although many popular HDC implementations use binary models with more hyperdimensions due to the hardware friendliness of the binary operations, binary models reduce accuracy; therefore, to demonstrate the efficient multi-bit operation capability of photonics, we use the above-mentioned bit-precision and  $D$  [34] [31].

## V. EVALUATION RESULTS

### A. Impact of $R$ and $C$ on Power Consumption

To better understand the nuances of the evaluation results, we first build the intuition about how different photonic unit sizes affect power consumption. In this regard, we summarize the changes in power consumption for different components of the microarchitecture when we double the number of rows (i.e., design a tall photonic unit) vs. the number of columns (design a wide photonic unit). In both cases, the latency is halved, but due to the interplay of different power components, especially the MZMs and the lasers, one design gets better than the other in terms of energy efficiency.

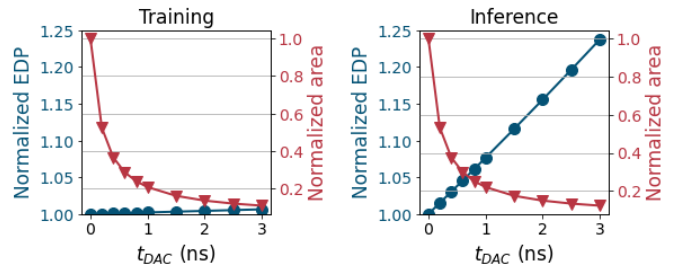


Fig. 7: Average EDP and the corresponding area for different extra DAC delays on a  $128\times 128$  core running at 5 GHz in the traditional encoding scheme. A small increase in EDP with a forced DAC delay can drastically decrease area, especially for training.

### B. Impact of $t_{DAC}$ on Area and EDP

We begin with an evaluation of the sensitivity of EDP and area to the extra delay we introduce in the DAC for traditional encoding. To demonstrate the benefit of this delay, we plot the EDP and area (see Figure 7) for different delay amounts for PhotoHDC with a  $128\times 128$  photonic unit running at 5 GHz as an example. On the left side, we can see that even a small delay of 1 ns can reduce the area by  $\approx 80\%$  with  $<1\%$  increase in EDP. The change in EDP with the increase in  $t_{DAC}$  is minimal because we switch a tile after every  $D$  ( $\approx 10^3$ ) cycles during training, and the 1 ns delay, i.e., 5 cycles, is insignificant compared to that. However, within these 5 cycles, one DAC can control  $5\times$  more PDs than before. As a result, we need less number of DACs and can achieve a significant area reduction.

For inference too, applying  $t_{DAC}$  helps reduce area without compromising too much on EDP, although to a lesser extent than for training. This is because tile switching occurs more frequently during inference than training. Additionally, we perform both encoding and similarity checking in the same photonic core, resulting in the delay affecting both stages. Despite this, the area reduction is substantial and contributes to efficient resource utilization.

### C. Energy-Delay-Area Product (EDAP)-optimized design

We explore the design space for each encoding scheme with an exhaustive search and find the architectural parameters that minimize the average EDAP over all the datasets that we have considered. We list the parameters and their power and performance in Table III. We use these parameters for power and area breakdown analysis in the later subsections. In general, we derive the following key insights based on the choice of the design parameters:

**First**, having a tall photonic unit is more energy-efficient than a wide one. This is because, for a column of PDs, the MZM power is higher than the power in the laser source that drives the PDs. More details about this tradeoff are provided in the next subsection.

**Second**, For record-based encoding (same as graph encoding) a smaller photonic unit is preferred than that for traditional encoding. Record-based encoding is power-hungry

TABLE III: Latency and power for the parameters ( $R \times C$ , number of photonic units,  $f$ ,  $t_{DAC}$ ) that minimize EDAP for training and inference under 20 W power and 500  $mm^2$  area.

Enc. type	Datasets	Training			Inference (1 million)		
		Params	Latency (ms)	Power (W)	Params	Latency (ms)	Power (W)
Traditional	ISOLET	$128 \times 76$ ,	0.09	4.8	$128 \times 128$ ,	8.71	10.3
	UCIHAR	4 units,	0.08	4.84	4 units	8.54	10.12
	FACE	5 GHz,	6.7	4.94	5 GHz	8.41	10.34
	PAMAP	1 ns	0.98	4.92	1 ns	1.8	9.32
	PECAN		0.18	4.7		5.1	9.97
Record	ISOLET	$128 \times 12$	0.7	19.41	$108 \times 12$	122.45	18.4
	UCIHAR	3 units	0.63	19.45	3 units	110.04	18.61
	FACE	5 GHz	56.85	19.6	5 GHz	117.94	18.81
	PAMAP		9.13	17.66		20.69	13.5
	PECAN		1.24	19.64		59.44	19.13
Graph	DD	$108 \times 12$ ,	0.07	16.42	$96 \times 48$ ,	52.14	19.86
	ENZYMES	3 units,	0.005	14.28	1 unit,	9.85	12.52
	PROTEINS	5 GHz	0.01	13.16	5 GHz	9.14	16.08

due to frequent tile switching. Therefore, having a small PD array, which requires less data loading per cycle, lowers power.

**Third**, running at the maximum frequency is a priority for getting the maximum benefit from a photonic unit. In our design, 5 GHz is the highest possible frequency because our chosen ADC operates at 5 GS/s. Unless bounded by a low power constraint or a bottleneck element that restricts the operating frequency, the best frequency choice would be the highest one. In all the chosen designs, the operating frequency is 5 GHz.

#### D. Power Breakdown of PhotoHDC

In Figure 8, we show the power breakdown for training and inference with different encoding schemes. We choose the design parameters listed in Table III for each plot. We show the breakdowns for the dataset ISOLET in traditional and record-based encoding and DD for graph encoding. The breakdown trends are similar in other datasets with small variations.

MZM tuning is the dominant power-consuming source for traditional encoding contributing more than 50% of the total power consumption. Usually, in the electro-photonic accelerators, we find that the ADCs and the lasers are the primary power consumers. However, both the laser power and ADCs contribute little to our design. The laser power is low due to the low SNR requirement for HDC and fewer losses in the optical path in our design. The ADCs for both training and inference have a low bit precision and in training, we only use one ADC per photonic unit for our efficient bundling strategy. Therefore, the MZM tuning power becomes the bottleneck in the design. SRAM data movement is also another major power-consuming source, contributing  $\approx 23\%$  to the total power consumption. For inference with traditional encoding, we need to use adders and TIAs of all the rows, so they contribute a good percentage to the power consumption as well.

In record-based encoding, the tile switching in every cycle results in the SRAM power consumption being dominant. The second-most power-consuming source is the MZM tuning circuit, and the other contributions are minimal. We find the same trends for graph encoding as well because it follows the same procedure as record-based encoding.

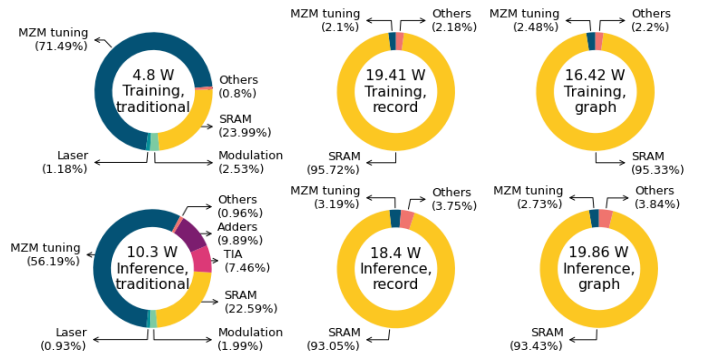


Fig. 8: Power breakdown of HDC training and inference for different encoding schemes. The design parameters minimize average EDAP and are listed in Table III.

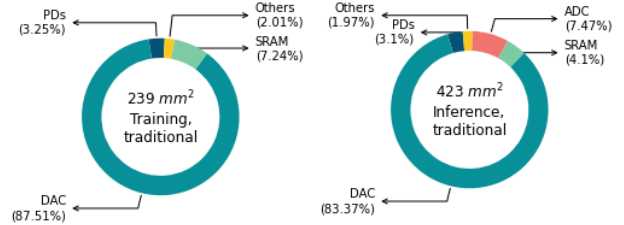


Fig. 9: Area breakdown of HDC training and inference with PhotoHDC. The design parameters are from Table III.

#### E. Area Breakdown of PhotoHDC

In Figure 9, we show the area breakdown of training and inference with traditional encoding with the architecture parameters (see Table III) that minimize EDAP for ISOLET. The breakdown trends are similar in other datasets and other encoding schemes with small variations caused by the size of the SRAM. The dominant area bottleneck for both training and inference is the DACs. Each DAC consumes significantly more area than a PD and the DACs account for  $\approx 83\text{--}87\%$  area of the chip. For inference, every row of a photonic unit uses an ADC, whereas in training only one ADC is used per photonic unit. Consequently, ADC contribution constitutes  $\approx 7\%$  of the area in inference but is negligible in training. The other contributors are MZMs and adders (and ADCs for training), consuming  $\approx 2\%$  of the area. If one wants a single PhotoHDC design that supports both training and inference, then one will need to use the design parameters for inference from Table III.

#### F. Iso-area and Iso-power Analysis

In this section, for each encoding scheme, we perform an exhaustive search to find the design configuration that minimizes the average EDP over the datasets for different resource (power/area) budgets. We first plot the normalized average EDP for different power budgets with a fixed 500  $mm^2$  area constraint in Figure 10. We can observe that the EDP for record-based encoding saturates slowly, meaning that with this encoding and the associated dataflow, the accelerator can leverage the increasing power budget. This is because the record-based encoding is power-hungry due to frequent data loading from the SRAM and so it needs to run on smaller

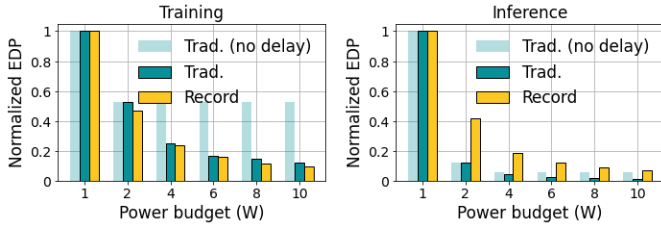


Fig. 10: Best average EDP (normalized) for different encoding schemes for different power budgets. The area budget is 500  $mm^2$ . The EDP for traditional encoding with no extra DAC delay saturates quickly. The EDP for record-based encoding and traditional encoding with extra DAC delay saturate slower.

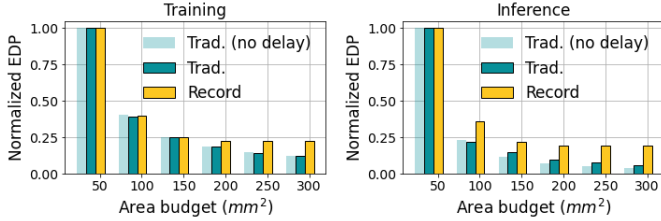


Fig. 11: Best average EDP (normalized) for different encoding schemes for different area budgets. The power budget is fixed at 20 W. Record-based encoding saturates faster than traditional encoding.

photonic units to save power when the power budget is low. Allocating a higher power budget allows for larger photonic units and faster execution for both training and inference, resulting in a slow saturation rate. On the other hand, the EDP for traditional encoding with no delays saturates quickly because it consumes a large area even at low power consumption due to the huge number of DACs being inactive most of the time. Allowing the extra delay in traditional encoding helps to slow down saturation by allowing for expansion in the computing resources (PDs and MZMs) while reducing the number of DACs.

In Figure 11, we plot the normalized EDP for different area budgets with a fixed 20 W power constraint. Here, record-based encoding saturates faster because its power consumption uses up the available power budget even for smaller designs i.e. low area. However, for traditional encoding, the increased area is utilized without crossing the power constraint. The extra DAC delay does not make any difference in this case because we are not limited by area.

The key takeaway from our analysis is that record-based encoding is power-hungry, so having a higher power budget is beneficial for it. For traditional encoding, the bottleneck is the area. Therefore, a larger area is beneficial for achieving better energy efficiency.

### G. Comparison with SOTA Electro-Photonic DNN Accelerator

Table IV shows a detailed comparison of the three SOTA electro-photonic DNN accelerators and PhotoHDC for performing HDC training and inference with traditional encoding. We do not compare the record-based encoding for the SOTA

accelerators, as they are all inefficient for this encoding scheme. We use the architectural configurations prescribed in the corresponding papers of the SOTA accelerators. For PhotoHDC, we use the parameters mentioned in Table III that minimize EDAP. For calculating area efficiency, we use the area of the active computing elements and the data converters for all accelerators for a fair comparison.

For all datasets, we observe that PhotoHDC achieves lower latency and lower power than other accelerators for both training and inference. ADEPT shows the closest performance to PhotoHDC for training and inference, but it still has 3-4 $\times$  higher latency. The power consumption is also higher in ADEPT than PhotoHDC, primarily due to the substantial laser power that supports the long chain of MZIs in its photonic core, and the higher bit-precision of the ADCs and DACs. DEAP-CNN is efficient in training if the data fits efficiently into its banks. However, because the MRRs introduce crosstalk and the tuning circuits are costly, it is challenging to design large MRR banks. The total number of computing elements (MRRs) in DEAP-CNN is much smaller than ADEPT (MZIs) and PhotoHDC (PDs), even though it consumes the highest power. As a result, the latency of DEAP-CNN is at least one order of magnitude higher than PhotoHDC. ALBIREO has the highest latency among all accelerators because it is highly optimized for CNNs and is not suitable for hyperdimensional computing.

Overall, on average, for training PhotoHDC achieves three orders of magnitude lower EDP and one order of magnitude better efficiency (throughput/power/area) than the SOTA electro-photonic accelerators. In inference too, PhotoHDC achieves at least two orders of magnitude lower EDP and one order of magnitude better efficiency than the SOTA electro-photonic accelerators. It should be noted that the efficiency improvement of PhotoHDC over ADEPT is better for inference than training. This is because, in inference, the CHV matrix shape is narrow ( $K \times D$ ), and a square  $128 \times 128$  MZI array of ADEPT wastes a lot of area when mapping the CHV matrix. Having the flexibility on the shape of the photonic unit is a key advantage for PhotoHDC to be more suitable for HDC than a square MZI-array-based accelerator, especially for inference.

### H. Comparison with CiM-based Accelerator

Table V shows the comparison between PhotoHDC and CiM for training and inference for traditional encoding. As Neurosim 2.1 doesn't support bit-precision of less than 5 bits for training, we set the bit-precision to 5 for both CiM and PhotoHDC. The hyperdimension remains the same at 4096. Similar to our previous experiments, we choose the configuration that minimizes the EDAP for PhotoHDC.

Primarily, due to the fast and energy-efficient multi-bit analog computing capability of photonics, PhotoHDC achieves three orders of magnitude speedup over CiM-based accelerator. In the CiM approach, multi-bit MVM operations in the ReRAM arrays make the encoding process slow. On top of that, due to the lack of an efficient batch processing

TABLE IV: Comparison of SOTA electro-photonic accelerators: ADEPT (AD) [10], DEAP-CNN (DC) [7], and ALBIREO (AL) [53] with PhotoHDC (PH) for HDC training (top) and inference (bottom) using one million samples with traditional encoding.

Training																
Datasets	Latency (ms)				Power (W)				EDP (Js)				Efficiency (Sample/s/W/mm <sup>2</sup> )			
	AD	DC	AL	PH	AD	DC	AL	PH	AD	DC	AL	PH	AD	DC	AL	PH
ISOLET	0.28	2.56	4.36	0.09	13.67	100	60	4.8	1.04E-06	6.53E-04	1.14E-03	3.98E-08	1.07E+04	5.90E+03	2.05E+02	6.43E+04
UCIHAR	0.28	2.54	3.97	0.08	13.33	100	60	4.84	1.01E-06	6.48E-04	9.44E-04	3.13E-08	1.10E+04	5.90E+03	2.24E+02	7.19E+04
FACE	22.30	213.99	365.29	6.70	13.58	100	60	4.94	6.75E-03	4.58E+00	8.01E+00	2.21E-04	1.12E+04	5.90E+03	2.05E+02	7.11E+04
PAMAP	16.73	250.32	55.74	0.98	5.31	100	60	4.92	1.49E-03	6.27E+00	1.86E-01	4.72E-06	4.46E+04	5.90E+03	1.57E+03	5.71E+05
PECAN	0.62	9.13	8.13	0.18	12.27	100	60	4.7	4.65E-06	8.34E-03	3.97E-03	1.52E-07	1.91E+04	5.90E+03	3.92E+02	1.19E+05

Inference																
Datasets	Latency (ms)				Power (W)				EDP (Js)				Efficiency (Sample/s/W/mm <sup>2</sup> )			
	AD	DC	AL	PH	AD	DC	AL	PH	AD	DC	AL	PH	AD	DC	AL	PH
ISOLET	42.68	409.60	699.20	8.71	15.98	200	120	10.3	2.91E-02	3.36E+01	5.87E+01	7.82E-04	4.75E+03	1.47E+03	5.12E+01	2.75E+04
UCIHAR	42.68	409.60	638.40	8.54	15.57	200	120	10.12	2.84E-02	3.36E+01	4.89E+01	7.38E-04	4.88E+03	1.47E+03	5.60E+01	2.86E+04
FACE	42.68	409.60	699.20	8.41	15.76	200	120	10.34	2.87E-02	3.36E+01	5.87E+01	7.32E-04	4.82E+03	1.47E+03	5.12E+01	2.84E+04
PAMAP	8.54	409.60	91.20	1.80	19.81	200	120	9.32	1.44E-03	3.36E+01	9.98E-01	3.02E-05	1.92E+04	1.47E+03	3.92E+02	1.47E+05
PECAN	25.61	409.60	364.80	5.10	16.16	200	120	9.97	1.06E-02	3.36E+01	1.60E+01	2.59E-04	7.83E+03	1.47E+03	9.80E+01	4.85E+04

TABLE V: Comparison between CiM-based accelerator and PhotoHDC (PH) when performing training and inference.

Training						
Dataset	Training time (ms)		× Speed-up	Power (W)		Power ratio (EP/CiM)
	PH	CiM		PH	CiM	
ISOLET	0.09	94.76	1.05E+03	5.32	9.40E-03	5.66E+02
UCIHAR	0.08	92.64	1.16E+03	5.36	9.40E-03	5.70E+02
FACE	6.7	6892.52	1.03E+03	5.49	9.40E-03	5.84E+02

Inference						
Dataset	Throughput (inf/s)		× Speed-up	Power (W)		Power ratio (PH/CiM)
	PH	CiM		PH	CiM	
ISOLET	1.15E+08	7.56E+04	1.52E+03	11.50	1.24E-02	9.27E+02
UCIHAR	1.17E+08	7.74E+04	1.51E+03	11.29	1.25E-02	9.03E+02
FACE	1.19E+08	7.59E+04	1.57E+03	11.56	1.25E-02	9.25E+02

mechanism [39], the CiM-based accelerator experiences a high latency when handling a batch of samples. Also, the long update times of the CHVs in the ReRAM make the bundling step time-consuming. That is why, even though the CiM-based accelerator consumes very low power for both training and inference, the high speed-up in PhotoHDC leads to four orders of magnitude better energy efficiency for PhotoHDC.

## VI. RELATED WORK

For HDC operations, several CPU-based [24], [25], GPU-based [16], [28], [35], ASIC-based [32], [33], FPGA-based [22], [51], [52], and CiM-based [30], [31], [37], [63] accelerators have been proposed. The main objective of digital ASIC solutions is to optimize power consumption and area. The FPGA-based techniques generally concentrate on accelerating the encoding step with computation reuse and they have higher performance than the GPU-based implementations [52]. However, the FPGA resources, such as floating point units, DSP blocks, etc., are substantially more complex than what HDC requires—which calls for a more energy-efficient solution. That is why different CiM technologies have been extensively explored for HDC applications [8], [26], [29]. These works have demonstrated one or more orders of magnitude better energy efficiency and throughput compared to the aforementioned non-CiM designs for HDC.

Nevertheless, inefficient multi-bit operations, high write time, and low endurance issues are still the major challenges in CiM.

Over the past few years, researchers have explored the use of photonic computing for accelerating DNNs [7], [53], [56], [60]. These implementations demonstrated multiple orders of magnitude higher compute throughput than their electronic counterparts for GEMM operations. However, frequent non-linear operations in DNNs require extra digital electronic circuitry that is much slower than photonics. These non-linear operations are a bottleneck in the electro-photonic systems for DNNs and require careful system optimizations and tedious operation scheduling. Moreover, it is challenging to balance energy efficiency and DNN accuracy in an electro-photonic DNN accelerator. For both DNN inference and training, achieving high precision requires high SNR leading to high laser power and high-precision data converters. From an algorithmic standpoint, HDC is considerably simpler than DNNs, involving primarily linear operations and requiring low precision. This suggests that photonics is well-suited for HDC than DNNs. While HDC operations can be mapped onto existing electro-photonic DNN accelerators, they encounter low-utilization and over-complicated hardware issues, as discussed in detail in Sections IV and V. Therefore, a simplified design is necessary to efficiently support HDC in electro-photonic systems.

In this paper, we argue that HDC and silicon photonic technology are better suited for each other than other combinations. We design the very first electro-photonic systems to accelerate HDC training and inference supporting three popular encoding schemes. We also develop novel dataflows for training and inference with each encoding scheme. With a simpler design and optimized dataflows, our accelerator overcomes the limitations in existing electro-photonic DNN accelerators and also shows better performance and energy efficiency over the CiM-based approach.

## VII. CONCLUSION

In this work, we suggest that instead of DNN inference, silicon-photonic computing is more suitable for HDC, which achieves near-identical accuracy to DNNs in a variety of

applications. For the first time ever, we propose an electro-photonic accelerator PhotoHDC for HDC training and inference supporting three popular encoding schemes. With extensive experiments and comparisons, we show that for HDC training and inference, our accelerator can achieve at least two orders of magnitude lower EDP than SOTA electro-photonic DNN accelerators. PhotoHDC also achieves four orders of magnitude lower EDP than CiM-based accelerators for both HDC training and inference.

## REFERENCES

- [1] “Genus synthesis solution.” [https://www.cadence.com/en\\_US/home/tools/digital-design-and-signoff/synthesis/genus-synthesis-solution.html](https://www.cadence.com/en_US/home/tools/digital-design-and-signoff/synthesis/genus-synthesis-solution.html).
- [2] “GF22nm FD-SOI Technology,” <https://globalfoundries.com/sites/default/files/product-briefs/pb-22fdx-26-web.pdf>.
- [3] “Pecan street dataport,” <https://dataport.cloud/>.
- [4] S. Akiyama, T. Baba, M. Imai, T. Akagawa, M. Takahashi, N. Hirayama, H. Takahashi, Y. Noguchi, H. Okayama, T. Horikawa, and T. Usuki, “12.5-Gb/s operation with 0.29-V-cm  $V\pi L$  using silicon Mach-Zehnder modulator based-on forward-biased pin diode,” *Opt. Express*, 2012.
- [5] A. Angelova, Y. Abu-Mostafam, and P. Perona, “Pruning training sets for learning of object categories,” in *2005 IEEE Computer Society Conference on Computer Vision and Pattern Recognition (CVPR’05)*, vol. 1. IEEE, 2005, pp. 494–501.
- [6] D. Anguita, A. Ghio, L. Oneto, X. Parra, and J. L. Reyes-Ortiz, “A public domain dataset for human activity recognition using smartphones.” in *Esann*, vol. 3, 2013, p. 3.
- [7] V. Bangari, B. A. Marquez, H. Miller, A. N. Tait, M. A. Nahmias, T. F. de Lima, H.-T. Peng, P. R. Prucnal, and B. J. Shastri, “Digital electronics and analog photonics for convolutional neural networks (deap-cnns),” *IEEE Journal of Selected Topics in Quantum Electronics*, vol. 26, no. 1, pp. 1–13, 2020.
- [8] H. E. Barkam, S. Yun, P. R. Genssler, Z. Zou, C.-K. Liu, H. Amrouch, and M. Imani, “Hdgm: Hyperdimensional genome sequence matching on unreliable highly scaled fetef,” in *2023 Design, Automation & Test in Europe Conference & Exhibition (DATE)*. IEEE, 2023, pp. 1–6.
- [9] K. M. Borgwardt, C. S. Ong, S. Schönauer, S. Vishwanathan, A. J. Smola, and H.-P. Kriegel, “Protein function prediction via graph kernels,” *Bioinformatics*, vol. 21, no. suppl\_1, pp. i47–i56, 2005.
- [10] C. Demirkiran, F. Eris, G. Wang, J. Elmhurst, N. Moore, N. C. Harris, A. Basumallik, V. J. Reddi, A. Joshi, and D. Bunandar, “An electro-photonic system for accelerating deep neural networks,” *arXiv preprint arXiv:2109.01126*, 2021.
- [11] P. D. Dobson and A. J. Doig, “Distinguishing enzyme structures from non-enzymes without alignments,” *Journal of molecular biology*, vol. 330, no. 4, pp. 771–783, 2003.
- [12] D. Dua and C. Graff, “UCI machine learning repository,” 2017. [Online]. Available: <http://archive.ics.uci.edu/ml>
- [13] P. Edinger, A. Y. Takabayashi, C. Errando-Herranz, U. Khan, H. Sattari, P. Verheyen, W. Bogaerts, N. Quack, and K. B. Gylfason, “Silicon photonic microelectromechanical phase shifters for scalable programmable photonics,” *Optics Letters*, 2021.
- [14] L. Ge and K. K. Parhi, “Classification using hyperdimensional computing: A review,” *IEEE Circuits and Systems Magazine*, 2020.
- [15] M. Guo, J. Mao, S.-W. Sin, H. Wei, and R. P. Martins, “A 29nm 5gs/s time-interleaved sar adc achieving 48.5 db snr with fully-digital timing-skew calibration based on digital-mixing,” in *2019 Symposium on VLSI Circuits*. IEEE, 2019, pp. C76–C77.
- [16] Y. Guo, M. Imani, J. Kang, S. Salamat, J. Morris, B. Aksanli, Y. Kim, and T. Rosing, “Hyperrec: Efficient recommender systems with hyperdimensional computing,” in *Proceedings of the 26th Asia and South Pacific Design Automation Conference*, 2021, pp. 384–389.
- [17] N. C. Harris, “Photonics processor architecture,” Oct. 28 2021, uS Patent App. 17/240,506.
- [18] N. C. Harris, Y. Ma, J. Mower, T. Baehr-Jones, D. Englund, M. Hochberg, and C. Galland, “Efficient, compact and low loss thermo-optic phase shifter in silicon,” *Optics express*, 2014.
- [19] A. Hernandez-Cano, N. Matsumoto, E. Ping, and M. Imani, “Onlinehd: Robust, efficient, and single-pass online learning using hyperdimensional system,” in *IEEE DATE*, 2021.
- [20] H.-Y. Huang, X.-Y. Chen, and T.-H. Kuo, “A 10-gs/s nrz/mixing dac with switching-glitch compensation achieving  $sfd_{\text{r}}/64/50$  dbc over the first/second nyquist zone,” *IEEE Journal of Solid-State Circuits*, vol. 56, no. 10, pp. 3145–3156, 2021.
- [21] Z. Huang, C. Li, D. Liang, K. Yu, C. Santori, M. Fiorentino, W. Sorin, S. Palermo, and R. G. Beausoleil, “25 gbps low-voltage waveguide si-ge avalanche photodiode,” *Optica*, vol. 3, no. 8, pp. 793–798, 2016.
- [22] M. Imani, S. Bosch, M. Javaheripi, B. Rouhani, X. Wu, F. Koushanfar, and T. Rosing, “Semihd: Semi-supervised learning using hyperdimensional computing,” in *2019 IEEE/ACM International Conference on Computer-Aided Design (ICCAD)*. IEEE, 2019, pp. 1–8.
- [23] M. Imani, C. Huang, D. Kong, and T. Rosing, “Hierarchical hyperdimensional computing for energy efficient classification,” in *Proceedings of the 55th Annual Design Automation Conference*, 2018, pp. 1–6.
- [24] M. Imani, D. Kong, A. Rahimi, and T. Rosing, “Voicehd: Hyperdimensional computing for efficient speech recognition,” in *2017 IEEE international conference on rebooting computing (ICRC)*. IEEE, 2017, pp. 1–8.
- [25] M. Imani, J. Morris, S. Bosch, H. Shu, G. De Micheli, and T. Rosing, “Adapthd: Adaptive efficient training for brain-inspired hyperdimensional computing,” in *2019 IEEE Biomedical Circuits and Systems Conference (BioCAS)*. IEEE, 2019, pp. 1–4.
- [26] M. Imani, X. Yin, J. Messerly, S. Gupta, M. Niemier, X. S. Hu, and T. Rosing, “Searchd: A memory-centric hyperdimensional computing with stochastic training,” *IEEE Transactions on Computer-Aided Design of Integrated Circuits and Systems*, vol. 39, no. 10, pp. 2422–2433, 2019.
- [27] M. Imani, A. Zakeri, H. Chen, T. Kim, P. Poduval, H. Lee, Y. Kim, E. Sadredini, and F. Imani, “Neural computation for robust and holographic face detection,” in *DAC*, 2022.
- [28] J. Kang, B. Khaleghi, T. Rosing, and Y. Kim, “Openhd: A gpu-powered framework for hyperdimensional computing,” *IEEE Transactions on Computers*, vol. 71, no. 11, pp. 2753–2765, 2022.
- [29] G. Karunaratne, M. Le Gallo, G. Cherubini, L. Benini, A. Rahimi, and A. Sebastian, “In-memory hyperdimensional computing,” *Nature Electronics*, 2020.
- [30] A. Kazemi, F. Müller, M. M. Sharifi, H. Errahmouni, G. Gerlach, T. Kämpfe, M. Imani, X. S. Hu, and M. Niemier, “Achieving software-equivalent accuracy for hyperdimensional computing with ferroelectric-based in-memory computing,” *Scientific reports*, 2022.
- [31] A. Kazemi, M. M. Sharifi, Z. Zou, M. Niemier, X. S. Hu, and M. Imani, “Mimhd: Accurate and efficient hyperdimensional inference using multi-bit in-memory computing,” in *IEEE/ACM ISLPED*, 2021.
- [32] B. Khaleghi, J. Kang, H. Xu, J. Morris, and T. Rosing, “Generic: highly efficient learning engine on edge using hyperdimensional computing,” in *IEEE DAC*, 2022.
- [33] B. Khaleghi, H. Xu, J. Morris, and T. Š. Rosing, “tiny-hd: Ultra-efficient hyperdimensional computing engine for iot applications,” in *2021 Design, Automation & Test in Europe Conference & Exhibition (DATE)*. IEEE, 2021, pp. 408–413.
- [34] J. Kim, H. Lee, M. Imani, and Y. Kim, “Efficient hyperdimensional learning with trainable, quantizable, and holistic data representation,” in *2023 Design, Automation & Test in Europe Conference & Exhibition (DATE)*. IEEE, 2023, pp. 1–6.
- [35] Y. Kim, J. Kim, and M. Imani, “Cascadehd: Efficient many-class learning framework using hyperdimensional computing,” in *2021 58th ACM/IEEE Design Automation Conference (DAC)*. IEEE, 2021, pp. 775–780.
- [36] H. Li, W.-C. Chen, A. Levy, C.-H. Wang, H. Wang, P.-H. Chen, W. Wan, W.-S. Khwa, H. Chuang, Y.-D. Chih, M.-F. Chang, H.-S. P. Wong, and P. Raina, “Sapiens: A 64-kb rram-based non-volatile associative memory for one-shot learning and inference at the edge,” *IEEE Transactions on Electron Devices*, vol. 68, no. 12, pp. 6637–6643, 2021.
- [37] C.-K. Liu, H. Chen, M. Imani, K. Ni, A. Kazemi, A. F. Laguna, M. Niemier, X. S. Hu, L. Zhao, C. Zhuo, and X. Yin, “Cosime: Fetef based associative memory for in-memory cosine similarity search,” in *IEEE/ACM ICCAD*, 2022.
- [38] W. Liu, W. Liu, Y. Ye, Q. Lou, Y. Xie, and L. Jiang, “Holylight: A nanophotonic accelerator for deep learning in data centers,” in *2019 Design, Automation & Test in Europe Conference & Exhibition (DATE)*. IEEE, 2019, pp. 1483–1488.
- [39] A. Lu, X. Peng, W. Li, H. Jiang, and S. Yu, “Neurosim simulator for compute-in-memory hardware accelerator: Validation and benchmark,” *Frontiers in artificial intelligence*, vol. 4, p. 659060, 2021.



- [40] G. Mourou, B. Brocklesby, T. Tajima, and J. Limpert, "The future is fibre accelerators," *Nature Photonics*, 2013.
- [41] P. Neubert, S. Schubert, and P. Protzel, "An introduction to hyperdimensional computing for robotics," *KI-Künstliche Intelligenz*, 2019.
- [42] K. Ni, X. Yin, A. F. Laguna, S. Joshi, S. Dünkel, M. Trentzsch, J. Müller, S. Beyer, M. Niemier, X. S. Hu, and S. Datta, "Ferroelectric ternary content-addressable memory for one-shot learning," *Nature Electronics*, vol. 2, no. 11, pp. 521–529, 2019.
- [43] I. Nunes, M. Heddes, T. Givargis, A. Nicolau, and A. Veidenbaum, "Graphhd: Efficient graph classification using hyperdimensional computing," in *2022 Design, Automation & Test in Europe Conference & Exhibition (DATE)*. IEEE, 2022, pp. 1485–1490.
- [44] X. Peng, S. Huang, H. Jiang, A. Lu, and S. Yu, "Dnn+ neurosim v2. 0: An end-to-end benchmarking framework for compute-in-memory accelerators for on-chip training," *IEEE TCAD*, 2020.
- [45] X. Peng, S. Huang, Y. Luo, X. Sun, and S. Yu, "Dnn+ neurosim: An end-to-end benchmarking framework for compute-in-memory accelerators with versatile device technologies," in *2019 IEEE international electron devices meeting (IEDM)*. IEEE, 2019, pp. 32–5.
- [46] P. Poduval, H. Alimohamadi, A. Zakeri, F. Imani, M. Najafi, T. Givargis, and M. Imani, "Graphd: Graph-based hyperdimensional memorization for brain-like cognitive learning," *Front. Neurosci.* 16: 757125. doi: 10.3389/fnins, 2022.
- [47] M. Poot and H. X. Tang, "Broadband nanoelectromechanical phase shifting of light on a chip," *Applied Physics Letters*, 2014.
- [48] A. Rahimi, S. Datta, D. Kleyko, E. P. Frady, B. Olshausen, P. Kanerva, and J. M. Rabaey, "High-dimensional computing as a nanoscalable paradigm," *IEEE Transactions on Circuits and Systems I: Regular Papers*, vol. 64, no. 9, pp. 2508–2521, 2017.
- [49] M. Rakowski, Y. Ban, P. De Heyn, N. Pantano, B. Snyder, S. Balakrishnan, S. Van Huylenbroeck, L. Bogaerts, C. Demeurisse, F. Inoue *et al.*, "Hybrid 14nm finfet-silicon photonics technology for low-power tb/s/mm<sup>2</sup> optical i/o," in *2018 IEEE Symposium on VLSI Technology*. IEEE, 2018, pp. 221–222.
- [50] A. Reiss and D. Stricker, "Introducing a new benchmarked dataset for activity monitoring," in *2012 16th international symposium on wearable computers*. IEEE, 2012, pp. 108–109.
- [51] S. Salamat, M. Imani, B. Khaleghi, and T. Rosing, "F5-hd: Fast flexible fpga-based framework for refreshing hyperdimensional computing," in *ACM FPGA*, 2019.
- [52] S. Salamat, M. Imani, and T. Rosing, "Accelerating hyperdimensional computing on fpgas by exploiting computational reuse," *IEEE Transactions on Computers*, vol. 69, no. 8, pp. 1159–1171, 2020.
- [53] K. Shiflett, A. Karanth, R. Bunescu, and A. Louri, "Albireo: Energy-efficient acceleration of convolutional neural networks via silicon photonics," in *ACM/IEEE ISCA*, 2021.
- [54] K. Shiflett, D. Wright, A. Karanth, and A. Louri, "Pixel: Photonic neural network accelerator," in *2020 IEEE International Symposium on High Performance Computer Architecture (HPCA)*. IEEE, 2020, pp. 474–487.
- [55] C. Sun, M. T. Wade, Y. Lee, J. S. Orcutt, L. Alloatti, M. S. Georgas, A. S. Waterman, J. M. Shainline, R. R. Avizienis, S. Lin, B. R. Moss, R. Kumar, F. Pavanello, A. Atabaki, H. Cook, A. J. Ou, J. C. Leu, Y.-H. Chen, K. Asanović<sup>1</sup>, R. J. Ram, M. A. Popović<sup>3</sup>, and V. M. Stojanović<sup>1</sup>, "Single-chip microprocessor that communicates directly using light," *Nature*, vol. 528, no. 7583, pp. 534–538, 2015.
- [56] F. Sunny, A. Mirza, M. Nikdast, and S. Pasricha, "Crosslight: A cross-layer optimized silicon photonic neural network accelerator," in *2021 58th ACM/IEEE Design Automation Conference (DAC)*. IEEE, 2021, pp. 1069–1074.
- [57] F. P. Sunny, E. Taheri, M. Nikdast, and S. Pasricha, "A survey on silicon photonics for deep learning," *ACM Journal of Emerging Technologies in Computing System*, vol. 17, no. 4, pp. 1–57, 2021.
- [58] A. Thomas, S. Dasgupta, and T. Rosing, "Theoretical foundations of hyperdimensional computing," *Journal of Artificial Intelligence Research*, 2021.
- [59] C. Xu, D. Niu, N. Muralimanohar, R. Balasubramonian, T. Zhang, S. Yu, and Y. Xie, "Overcoming the challenges of crossbar resistive memory architectures," in *2015 IEEE 21st international symposium on high performance computer architecture (HPCA)*. IEEE, 2015, pp. 476–488.
- [60] X. Xu, M. Tan, B. Corcoran, J. Wu, A. Boes, T. G. Nguyen, S. T. Chu, B. E. Little, D. G. Hicks, R. Morandotti, A. Mitchell, and D. J. Moss, "11 tops photonic convolutional accelerator for optical neural networks," *Nature*, vol. 589, no. 7840, pp. 44–51, 2021.
- [61] J.-H. Yoon, M. Chang, W.-S. Khwa, Y.-D. Chih, M.-F. Chang, and A. Raychowdhury, "A 40-nm 118.44-tops/w voltage-sensing compute-in-memory rram macro with write verification and multi-bit encoding," *IEEE Journal of Solid-State Circuits*, vol. 57, no. 3, pp. 845–857, 2022.
- [62] H. Zhou, J. Dong, J. Cheng, W. Dong, C. Huang, Y. Shen, Q. Zhang, M. Gu, C. Qian, H. Chen, Z. Ruan, and X. Zhang, "Photonic matrix multiplication lights up photonic accelerator and beyond," *Light: Science & Applications*, 2022.
- [63] Z. Zou, H. Chen, P. Poduval, Y. Kim, M. Imani, E. Sadredini, R. Cammarota, and M. Imani, "Biohd: an efficient genome sequence search platform using hyperdimensional memorization," in *ACM/IEEE ISCA*, 2022.
- [64] Z. Zou, Y. Kim, F. Imani, H. Alimohamadi, R. Cammarota, and M. Imani, "Scalable edge-based hyperdimensional learning system with brain-like neural adaptation," in *ACM SC*, 2021.